Imaging wind field from videos: an innovative tool for urban scale measurements.

Annia Benchadi [1], Jairo Acuña Paz Y Miño [2]

[1] Univ. Lille, Univ. Littoral Côte d’Opale, ULR 4477 - TVES - Territoires Villes Environnement & Société, F-59000 Lille, France- annia.benchadi@univ-lille.fr

[2] Univ. Lille, Univ. Littoral Côte d’Opale, ULR 4477 - TVES - Territoires Villes Environnement & Société, F-59000 Lille, France- jairo.acuna-paz-y-mino@univ-lille.fr

Keywords: imagery, wind speed estimation, visual feature, optical flow, remote sensing

Abstract

This work presents an innovative image-based method for measuring wind speed and direction in urban environment using video footage. Wind dynamics are traditionally investigated at multiple spatial scales, including pollutant dispersion at the canopy level (Allwine, 2002), architectural design and outdoor comfort at the building scale (Allard & Ghiaus, 2012; Holst, 2011) and the convection heat transfer coefficient h [$Wm^{-2}K^{-1}$] used to define the boundary conditions of numerical simulations (Oke, 2017). In 1997, Gary Settles showed that image measurement could provide non-invasive and high-resolution measurements of fluid motion. This paper presents a method for extracting anemometric data from images, validated through a proof-of-concept. We process freely accessible videos from the internet in which air masses are identified at the canopy level. Motion extraction technique is used to isolate elements of the video that are in motion. This information is fed into an optical flow algorithm that estimates an apparent velocity in [pixels/frame]. To convert the data to [km/h], the view’s perspective is considered to ensure the conversion is accurate across the entire image. Distance mapping is performed by projecting the image onto a 3D model of the scene, and the camera's recording parameters are estimated by simulating the illumination of the scene. The anemometric data obtained are evaluated in relation to meteorological data recorded at a nearby weather station. Innovative and simple to implement, this approach provides estimates of wind speeds and directions that are both reliable and directly usable for architectural design and climate studies.

1. Introduction

Observing physical fields in the city contributes to a better understanding of urban space. Knowing how air masses move through the city would be essential to assessing the potential for natural ventilation (Settles, 1997). Wind speed, direction, and temperature in the streets are important factors in determining the size of openings to ensure effective ventilation (Georgakis, 2006; Allard & Ghiaus, 2012). On a smaller scale, the air velocity at the surface of buildings can provide information on energy losses through the envelope and feed into the boundary conditions for numerical simulations (Oke, 2017). In addition to the architectural design of cities, wind speeds are also relevant to health (Hargather, 2010) and environmental management (Cao, 2015).

To assess wind loading or wind-related factors in building design, meteorological data is generally used (Georgakis, 2006). They are collected from weather stations located near airports, away from any obstructions. However, wind characteristics in the city are different due to its complex structure and the variety of materials used, which alter the airflow dynamics of the scene.

To quantify wind, there are two opposing philosophies: either we adopt an Eulerian approach, using a fixed object to intercept the flow and determine its speed and direction; or we adopt a Lagrangian approach, tracing the trajectory of a moving air particle. Traditionally, the former (Eulerian) is preferred for ground measurements, while the latter (Lagrangian) is reserved for studying wind at altitude (Carrega, 2008). For architectural planning, the required accuracy of wind speed is of the order of 0.1 m/s (Georgakis, 2006).

For a long time, the use of *in situ* measuring instruments has been the standard, widely documented method for determining wind speeds and directions at various scales, for example: on the surface of buildings (Hagishima, 2003) to estimate a convection coefficient, 2 m above ground level (Holst, 2011) for pedestrian comfort, and in urban areas to describe their roughness, (Gál, 2009).

The major challenge of urban instrumentation lies in the judicious placement of sensors (Oke, 2017). Indeed, there is no established protocol to guide the installation of sensors for the purpose of measuring a velocity field (Palyvos, 2008). To ensure satisfactory measurement resolution at the urban scale, a large number of sensors would be required. However, this increase faces practical and methodological constraints. Measurement bias is caused, in particular, by the disruption of airflow due to the presence of instruments. Furthermore, the point-based nature of these measurements makes it difficult to represent the spatial distribution of a velocity field (Kegerise & Settles, 2000; Rehman, 2014).

More recently, a new strategy involves using drones with onboard sensors to collect wind speed and direction data in the city (Pu, 2023). Drones offer the ability to cover a large data acquisition area due to their ease of handling, the lightness of their onboard equipment, and their ability to observe complex geometry (Patrikar, 2020). However, a major challenge lies in the fact that data is collected sequentially (and not simultaneously), requiring temporal variations in wind to be considered during analysis (Ingenhorst, 2021).

An alternative strategy for measuring air velocity in cities involves the use of seeding techniques. (Allwine, 2002) proposes to assess carbon monoxide emissions above the Salt Lake City

This contribution has been peer-reviewed. The double-blind peer-review was conducted on the basis of the full paper.
https://doi.org/10.5194/isprs-annals-XI-3-2026-27-2026

canopy by dispersing a non-toxic artificial tracer and measuring its movement using a camera. In certain situations, the use of particles is difficult to implement due to their invasive nature (Hargather, 2011).

Given the diversity of existing wind measurement techniques and the inherent limitations of each (complexity of deployment, invasive nature of particles, lack of standardization of protocols), it is imperative to develop new solutions. In this context, this work presents an innovative and non-intrusive methodology aimed at providing reliable, and easily usable data of wind speed, thereby transforming our ability to model and design more resilient urban environments.

2. Method

We present an imaging measurement method that allows wind speed and direction data to be extracted in urban environments. This technique uses video footage recorded with a fixed framing, freely available online. The approach developed in this paper is based on two main methodological components. The first is the application of a motion extraction technique for image processing, whose role is to isolate moving elements and, in particular, to accentuate the visual signature of air masses containing particles (e.g. steam from chimneys and fog). The second component uses an optical flow algorithm to quantify the speed and determine the direction of movement of the identified air masses. To obtain quantitative and accurate anemometric measurements, a geometric calibration step is essential to convert pixel displacements, measured by optical flow, into physical speed units (e.g., km/h or m/s). This conversion requires consideration of the perspective of the view.

The depth and angle of the camera cause distortion in distance scales, meaning that the same movement in pixels does not represent the same actual speed depending on its position in the image. To remedy this, a distance map is created by projecting the 2D image onto a 3D model of the scene (Digital Elevation Model - DEM or equivalent). This modelling allows the actual distance represented by each pixel to be accurately determined for any point in the field of view. The intrinsic and extrinsic parameters of the camera (focal length, position, orientation) are thus estimated.

In order to assess the accuracy of the two-dimensional anemometric data (velocity and direction) obtained by image processing, a comparison with reference meteorological data recorded simultaneously is performed. The weather station is located in close proximity to the video field of view, ensuring the reliability and accuracy of the proposed method under real-world conditions.

2.1 Motion extraction treatment

Motion extraction is used to highlight subtle movements of elements in the scene. The process is based on two fundamental image processing operations: (1) normalized inversion of the colours of a reference image from the video footage, and (2) its fusion with the other images from the same video.

The first frame of the sequence I_t, with $t \in [0, T]$ is chosen as the reference image I_{ref} from the T images of the video footage. The resolution of these images is $N_x \times N_y$ pixels. At each pixel, intensity values are expressed in a normalized space defined over the domain [-1, 1], with the neutral point fixed at 0. At each pixel (x, y), a normalized colour inversion therefore corresponds to a simple change of sign, with I'_{ref} the transformed reference image such as:

$$I'_{ref}(x, y) = -I_{ref}(x, y) \quad (1)$$

The second operation consists in adding the image I'_{ref} to the other images of the video sequence I_t. The opacity factor $\alpha_{op} \in [0,1]$ determines the degree of transparency of images I'_{ref} and I_t in the final composition. For $\alpha_{op} = 0$, only image I_t is visible; for $\alpha_{op} = 1$, only image I'_{ref} is visible; and for $\alpha_{op} = 0.5$, both images I_t and I'_{ref} contribute equally to the visual synthesis. The addition of the two images is then a linear operation weighted by the opacity factor:

$$I_{add}(x, y) = \alpha_{op} . I'_{ref}(x, y) + (1 - \alpha_{op}) . I_t(x, y) \quad (2)$$

With I_{add}, the resulting image of the addition. By substituting $I'_{ref}(x, y) = -I_{ref}(x, y)$, we obtain the equation (3):

$$I_{add}(x, y) = (1 - \alpha_{op}) I_t(x, y) - \alpha_{op} I_{ref}(x, y) \quad (3)$$

In the case of our processing, α_{op} is fixed at 0,5. The relationship (3) becomes equation (4):

$$I_{add}(x, y) = 0.5(I_t(x, y) - I_{ref}(x, y)) \quad (4)$$

When $I_t(x, y) = I_{ref}(x, y)$, there is no change at the pixel(x, y) between the reference image and the image from the sequence. In this case, $I_{add}(x, y) = 0$, which corresponds to the absence of movement. When $I_t(x, y)$ differs from $I_{ref}(x, y)$, this results in a positive or negative deviation around the neutral value. Thus, the process acts as an amplifier of differences between immobile areas that converge toward neutral intensity and mobile areas that appear in sharp contrast with light or dark luminance depending on the direction of change.
Figure 1 shows the effect of processing on an image of fog moving over the city of Toronto. The shades of gray highlight its passage. The contrast provides a sharper outline of the air masses moving between the buildings.

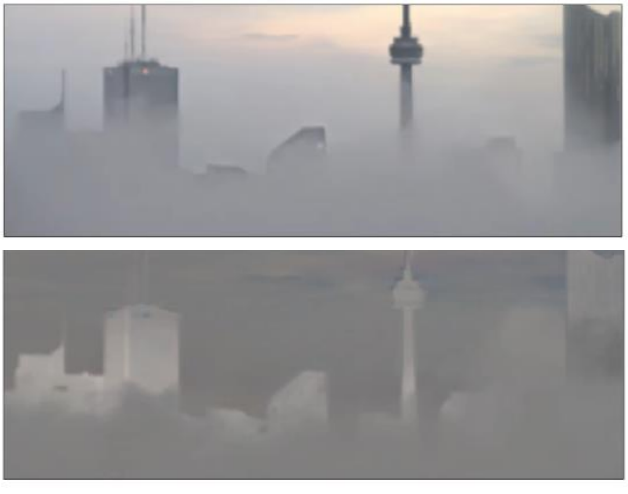

Figure 1. (1) Original frame. (2) Frame processed by motion extraction.

2.2 Optical flow

The optical flow designates a field of vectors that describes the movement of an object between two images (Fezzani, 2011). It is based on two main assumptions. The first suggests that the

intensity of the tracked object remains constant between two frames:

$$I(x + \delta x, y + \delta y, t + \delta t) - I(x, y, t) = 0 \quad (5)$$

With I, the matrix containing the intensities at each pixel of the image with coordinates (x, y), $(\delta x, \delta y)$ the new coordinates of the object, t and δt are the time and the time step between two frames.

The second hypothesis considers small movements allowing the object to be tracked. The works of (Horn & Schunck, 1981) and (Kanade, 1981) present an approximate version of the intensity conservation condition (equation (5)) by deriving the light intensity over time, given by equation (6):

$$\frac{\partial I}{\partial t} + \frac{\partial I}{\partial x}.\frac{dx}{dt} + \frac{\partial I}{\partial y}.\frac{dy}{dt} = 0 \quad (6)$$

With $\left(\frac{dx}{dt}, \frac{dy}{dt}\right)$ the velocity at pixel (x, y). The fundamental constraint of optical flow is described by the equation (7):

$$\partial_t I + \partial_x I.u + \partial_y I.v = 0 \quad (7)$$

Where $\partial_* I$ corresponds to the partial derivatives of I with respect to the variables (x, y, t), and (u, v) designate the desired optical flow expressed in [pixels/frame]. To solve equation (7), (Horn & Schunck, 1981) and (Kanade, 1981) provide formulations that assume small displacements of the object between images. In fact, the optical flow constraint is obtained from a Taylor expansion that applies when the displacements (dx, dy) are small enough to be neglected:

$$I(x + u, y + v, t + 1) \approx I(x, y, t + 1) + \partial_x I.u + \partial_y I.v = I(x, y, t) \quad (8)$$

The images studied in this paper were acquired in time-lapse format, which results in large displacements of the analysed objects between frames. The formulations proposed by (Horn & Schunck, 1981) and (Kanade, 1981) are limited in this case, as they are only correct for small displacements. In what follows, we note:

$$\mathbf{x} = (x, y, t) \quad (9)$$

$$\mathbf{u} = (u, v, t) \quad (10)$$

Where $\mathbf{x}$ and $\mathbf{u}$ are the position and the velocity vectors at time t. (Anandan, 1989) considers the problem at several resolution scales. The process begins at the coarsest level, where displacements are smallest and the Taylor expansion holds (Fezzani, 2011). A so-called *coarse-to-fine* strategy is employed, which consists in reducing the image resolution, defining a displacement at the coarsest resolution, and iterating the process while progressively increasing the image resolution toward a finer scale. The solution obtained at a given scale is used to initialize the problem at the next finer scale. In the literature, the technique is commonly referred to as *warping*, see Figure 2. This technique consists in iteratively repeating the development (8) by introducing a sequence $(\mathbf{u}^n)$ defined as follow:

$$\mathbf{u}^n = (u^n, v^n, t^n) \quad (11)$$

$$\mathbf{u}^{n+1} = \mathbf{u}^n + \delta\mathbf{u}^n \quad (12)$$

Where $\delta\mathbf{u}^n = (\delta u^n, \delta v^n, 0)$. We then obtain:

$$I(\mathbf{x} + \mathbf{u}^{n+1}) = I(\mathbf{x} + \mathbf{u}^n + \delta\mathbf{u}^n) = I(\mathbf{x} + \mathbf{u}^n) + \partial_x I(\mathbf{x} + \mathbf{u}^n).\delta u^n + \partial_y I(\mathbf{x} + \mathbf{u}^n).\delta v^n = I(\mathbf{x}) \quad (13)$$

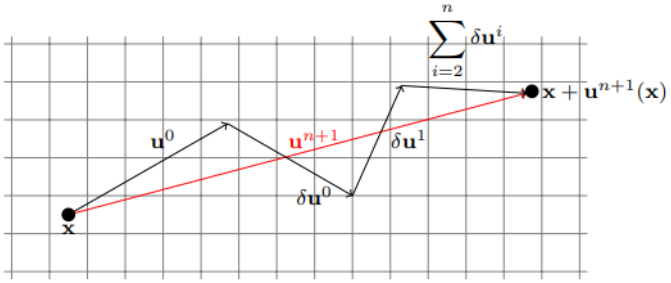

Figure 2. Schematic representation of the *warping* concept for large displacement estimation (Fezzani, 2011).

The algorithm employed in this study was developed during a PhD thesis at MIT by (Liu, 2009). The apparent velocity is then calculated from the output of the algorithm as follows:

$$V_{app} = \sqrt{u^2 + v^2} \quad (14)$$

Where V_{app} is the apparent velocity expressed in [pixels/frame], u and v denote the optical flow velocities along the $\vec{x}$ et $\vec{y}$ directions respectively expressed in [pixels/frame]. The direction is visually represented by showing the vector contributions of u and v.

2.3 Parameters of optical flow

The optical flow parameters are adjusted to avoid over- or under-estimation of the measured displacements. (Liu, 2008) proposes an automated parameter adjustment tool applied to the movement of rigid non-deformable objects. In our case, the air masses show significant deformations over time, which requires manual adjustment of the parameters.
A clearly visible air mass is identified on the video previously processed by motion extraction, see Figure 3. Two consecutive images are extracted in order to manually measure the displacement of the air mass between two acquisitions.

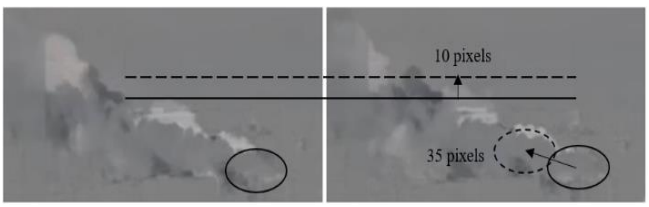

Figure 3. Manual measurement of the displacement between air mass images.

The first parameter studied is α that « smooths » the measured field. This results in continuous spatial variations and small amplitudes of the displacement vectors. The second parameter is the *downsampling ratio* (*ds ratio*), the degradation factor of the resolution of the images between each iterative step.
A sensitivity study is conducted to vary the parameters α and *ds ratio* independently. First, *ds ratio* is set to 0.75 for $\alpha \in$[0.012, 0.009, 0.008, 0.007, 0.006], see left column, Figure 4. Second, we set α to 0.008 while *ds ratio* $\in$ [0.9, 0.6, 0.5, 0.4, 0.3], see right column, Figure 4.

This contribution has been peer-reviewed. The double-blind peer-review was conducted on the basis of the full paper.
https://doi.org/10.5194/isprs-annals-XI-3-2026-27-2026 | © Author(s) 2026. CC BY 4.0 License.

When α decreases, the measured displacements are amplified. This is because displacement measurement is sensitive to even the slightest change in brightness. Conversely, increasing the smoothing parameter makes the measurement less sensitive to changes in brightness. We identify the coefficient $\alpha = \mathbf{0.008}$, which allows us to calculate the displacement field closest to the manual measurement.
When the *ds ratio* decreases, the measured displacements are amplified. For a *ds ratio* factor of 0.3, the two objects intersect due to excessive under sampling, resulting in an overestimation of the displacement. For values between 0.4 and 0.6, there is virtually no displacement due to the superimposition of the air masses.

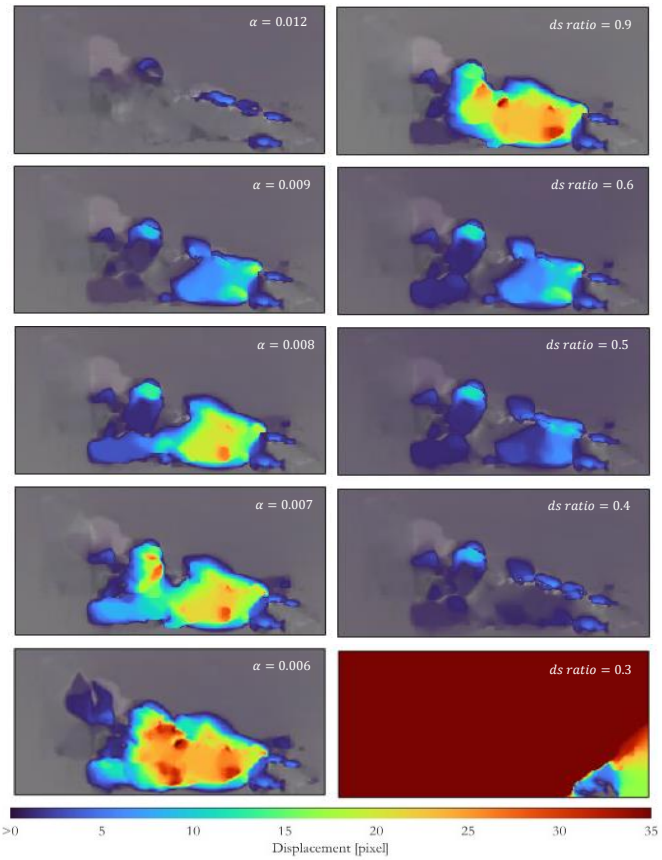

Figure 4. Sensitivity analysis to estimate parameter set [α, *ds ratio*].

In the case of this sequence studied, *ds ratio* = **0.9** offers a satisfactory compromise between progressive image degradation and accurate displacement estimation.
This step is repeated for each wind speed measurement.

2.4 Speed unit conversion

To evaluate the apparent velocity data obtained using the optical method, meteorological data is used as a reference. As this data is expressed in [km/h], the optical flow data, initially expressed in [pixels/frame], is converted into the same unit. Two conversions are required: (1) spatial conversion of the apparent distance [pixel] to [km], and (2) temporal conversion of the increment [frame] at real time to [h] between each frame.
Using Blender software, we import or create a 3D model of the city. In our case, we use the 3D model of the city of Toronto available online (City of Toronto, n.d.).
A virtual camera is positioned in the same location as the camera that captured the images *in situ*. Its position and orientation are adjusted by projecting an image extracted from the video into its field of view.
To determine the area covered by each pixel, a ray is cast that projects the area of each pixel onto the 3D model.
We begin by defining the intrinsic parameters of the camera with a focal length f in [mm], a sensor width S_x and S_y in [mm] and an image resolution $N_x \times N_y$ in [pixel]. The field of view (*Field of View, FOV*) is expressed as follows:

$$\Theta_x = 2\arctan\left(\frac{S_x}{2f}\right);\ \Theta_y = 2\arctan\left(\frac{S_y}{2f}\right) \tag{15}$$

With each pixel (x, y) corresponding to the elementary angles $\Delta\Theta_x = \frac{\Theta_x}{N_x}$, $\Delta\Theta_y = \frac{\Theta_y}{N_y}$. A first extrinsic parameter is defined by the world-to-camera transformation matrix:

$$M_c = \begin{bmatrix} R & t \\ 0 & 1 \end{bmatrix} \tag{16}$$

Where R is the rotation matrix and t is the camera translation in the world. The second extrinsic parameter is the position of the camera's optical center:

$$\boldsymbol{o_c} = M_c^{-1}(0,0,0,1)^T \tag{17}$$

In a second step, a viewing radius is defined for each pixel (x, y) by:

$$r_{x,y}(t) = o_c + t.\boldsymbol{d_{x,y}}\ , t > 0 \tag{18}$$

With $\boldsymbol{d_{x,y}}$ the direction of the ray obtained from the normalized coordinates of the pixel:

$$x_n = \frac{x + 0.5}{N_x} - 0.5\ ;\quad y_n = \frac{y + 0.5}{N_y} - 0.5 \tag{19}$$

Where x_n and $y_n \in [-0.5, 0.5]$. And field of vision:

$$\boldsymbol{d_{x,y}^{(cam)}} = \begin{bmatrix} \tan\left(\frac{\Theta_x}{2}\right).2x_n \\ -\tan\left(\frac{\Theta_y}{2}\right).2y_n \\ -1 \end{bmatrix} \tag{20}$$

Where the factors $\tan\left(\frac{\theta_x}{2}\right)$ and $\tan\left(\frac{\theta_y}{2}\right)$ convert the normalized coordinates to real field of view coordinates. Then:

$$\boldsymbol{d_{x,y}} = R.\frac{\boldsymbol{d_{x,y}^{(cam)}}}{\left\|\boldsymbol{d_{x,y}^{(cam)}}\right\|} \tag{21}$$

Thirdly, we consider a triangular mesh that represents the object targeted by the ray. For each pixel (x, y), we calculate the intersection data:

$$\left(hit, p_{x,y}, n_{x,y}\right) = \text{ray\_cast}\left(\boldsymbol{o_c}, \boldsymbol{d_{x,y}}\right) \tag{22}$$

Where $hit \in \{0,1\}$ indicates the presence of an intersection, $p_{x,y}$ is the intersection point, $n_{x,y}$ is the local normal to the surface at that point, and ray_cast() is the ray casting function. The projected area per pixel is then calculated based on the distance from this impact point to the camera:

$$\boldsymbol{d_{x,y}} = \left\|p_{x,y} - \boldsymbol{o_c}\right\| \tag{23}$$

https://doi.org/10.5194/isprs-annals-XI-3-2026-27-2026

According to the small angle assumption, the size of the pixel projected onto the image plane becomes:

$$\Delta x = 2\boldsymbol{d_{x,y}} \tan\left(\frac{\Delta\Theta_x}{2}\right); \quad \Delta y = 2\boldsymbol{d_{x,y}} \tan\left(\frac{\Delta\Theta_y}{2}\right) \tag{24}$$

We incorporate the calculation of the angle of incidence:

$$\cos(\alpha_{x,y}) = \left|\boldsymbol{d_{x,y}} \,.\, n_{x,y}\right| \tag{25}$$

The effective area projected onto the visible surface then becomes:

$$A_{x,y} = \frac{\Delta x.\Delta y}{\cos(\alpha_{x,y})}, \quad \text{if } \cos(\alpha_{x,y}) > \epsilon \tag{26}$$

With ϵ a numerical stability threshold and $A_{x,y} = 0$ if $\cos(\alpha_{x,y}) < \epsilon$. Under the assumption that each pixel is a perfect square, the scale ratio matrix $\boldsymbol{R_e}$ is derived from the surface matrix $A_{x,y}$ by calculating the diagonal of each pixel:

$$\boldsymbol{R_e}(x,y) = \sqrt{2.A_{x,y}} \tag{27}$$

The $\boldsymbol{R_e}$ matrix is represented graphically in Figure 5, image (2). It is used to evaluate the displacement of air masses circulating in the immediate vicinity of buildings. Due to perspective, the largest areas covered per pixel are at the back of the scene, while the smallest areas are those closest to the camera.

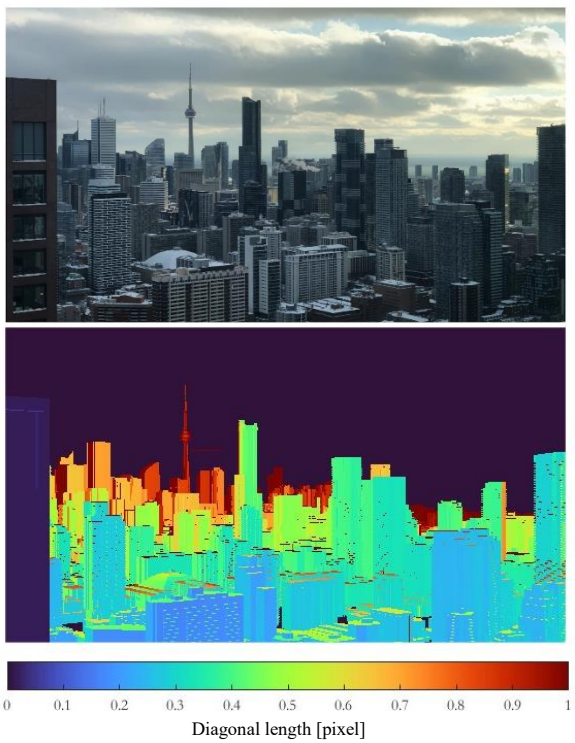

Figure 5. (1) Photograph of the scene. (2) Map showing diagonal length of each pixel of the scene under study.

The second conversion operation aims to transform the increment [frame] into real time step [h]. To determine the recording rate, we refer to the shadows cast on buildings. Two images are extracted from the video corresponding to two distinct moments i_1 and i_2 where the shadows are clearly identified on a facade, see Figure 6, images (1) and (2). In the 3D model, the position of the sun is simulated for the day the video was taken.
The simulated time h is adjusted manually to align the direction and shape of the shadows cast in the 3D model with those observed in the video. The actual times of moments i_1 and i_2 are then noted as t_1 and t_2.

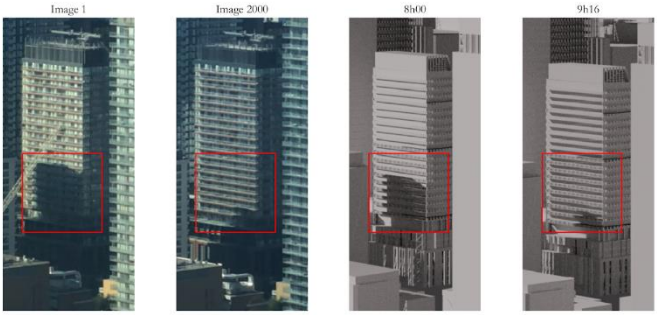

Figure 6. (1) and (2) Identification of two moments when the shadow is visible on a building. (3) and (4) Identification of the times corresponding to positions (1) and (2).

The recording rate c is calculated according to equation (28):

$$c = \frac{\Delta t_{real}}{\Delta i} \tag{28}$$

With $\Delta t_{real} = t_2 - t_1$ as the real time interval, and $\Delta i = i_2 - i_1$ as the number of images between the two selected moments.

2.5 Case study

In this paper, we propose to study air movements in the city of Toronto using videos posted online by (Carrillo, 2025). The images we use were recorded in time-lapse format, which allows us to visualize a daily phenomenon while using limited storage space. The camera is mounted on the window of an apartment, approximately 150 m above the ground.
The videos shot by (Carrillo, 2025) provide a large database of dated information. This allows reference to the historical meteorological data from the MeteoStat CXTO station located at spatial coordinates (43.67, -79.4). It records meteorological data from 112 m above sea level and is located 1.8 km west of the recording camera, see Figure 7.

Figure 7. Camera and MeteoStat station locations.

Table 1. Weather data recorded from the MeteoStat station in Toronto.

Date [month-day-year]	Time [h]	Speed [km/h]	Direction [-]	Temperature [°C]
02-13-25	9 a.m.	19.4	N/W	-7.7
02-13-25	10 a.m.	21.2	N/W	-8.5
02-13-25	11 a.m.	27	W	-8
02-13-25	12 p.m.	31.7	W	-8.4
02-13-25	1 p.m.	36	W	-8.9
02-13-25	2 p.m.	38.5	W	-9.1
02-13-25	3 p.m.	41.8	W	-9
02-13-25	4 p.m.	40.7	W	-8
05-16-25	9 a.m.	9	S/E	13

To compare these two measures, we analyse the temporal variations in speed and direction measurements over the course of a day.
Table 1 shows the speed and direction recorded by the MeteoStat station between 9 a.m. and 4 p.m. on February 13, 2025, and a measurement taken at 9 a.m. on May 16, 2025. These time periods were chosen because of the good visibility of the air masses observed by the camera.

3. Results

Two measurement results are presented. The first concerns the speed of the air evacuated from the city's chimneys, and the second shows the speed of the fog moving around buildings.

3.1 Measurement of air velocity in perspective view

Wind speed and direction are estimated based on the parameters determined previously.
To compare the orders of magnitude of the optical and anemometric measurements, a 10 x 10 pixels area (~16 m^2 of real surface) is extracted from the center of the plume, upstream of the flow. The average apparent velocity is calculated for this area. A sensibility analysis showed that the averaging area of 10 x 10 pixels minimizes bias with respect to the reference anemometric wind speed. The graph in Figure 9 shows that the average apparent velocities are of the same order of magnitude as those recorded by the weather station. However, there are differences between the values obtained by the two methods, which can be explained in several ways. On the one hand, the two devices record phenomena under different conditions. The camera measures flow in a high-density environment where the presence of buildings disrupts the flow. Conversely, the anemometer records data in a low-density environment. On the other hand, Figure 8 highlights velocity gradients within the measured fields. It is therefore possible to identify a measurement within the velocity field obtained by the optical method that would correspond to the anemometric data.

The velocities measured using the optical method are therefore realistic in terms of order of magnitude, allowing for a more detailed study of the spatial distributions of the velocity field. The velocity is always higher at the chimney outlet and at the center of the plume. These are the areas where the flow is more turbulent since the temperature is higher. When it mixes with the colder surrounding air (-7.7°C according to the weather station), the velocity of the plume decreases by about 70% compared to its maximum velocity. However, there is an exception for the 10 a.m. measurement, where the maximum velocity of the plume is located downstream of the flow. At this point in the sequence, the air plume exhibits different dynamic behaviour on either side of the central building. Downstream, the plume oscillates mainly vertically, while upstream, the plume is characterized by predominantly horizontal movements.

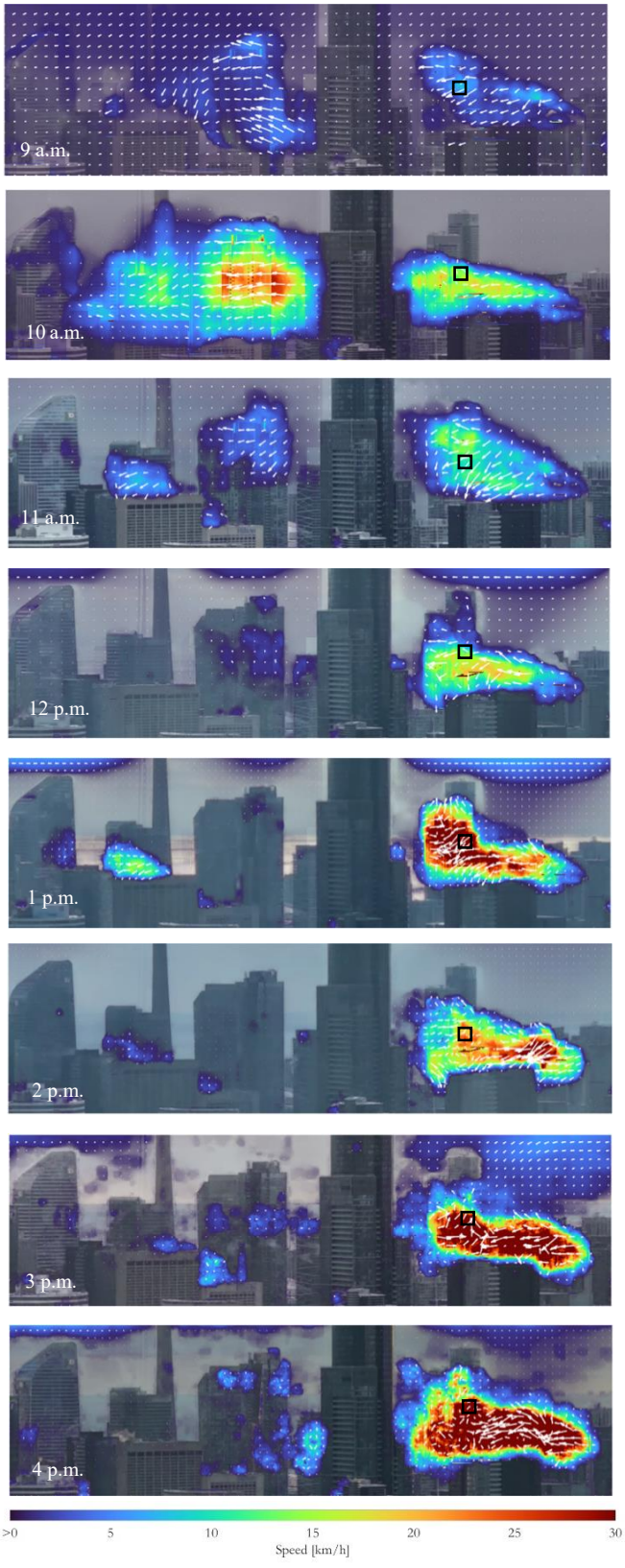

Figure 8. Air velocity and direction measured optically. (1) Measurement at 9 a.m. (2) 10 a.m. (3) 11 a.m. (4) 12 p.m. (5) 1 p.m. (6) 2 p.m. (7) 3 p.m. (8) 4 p.m.

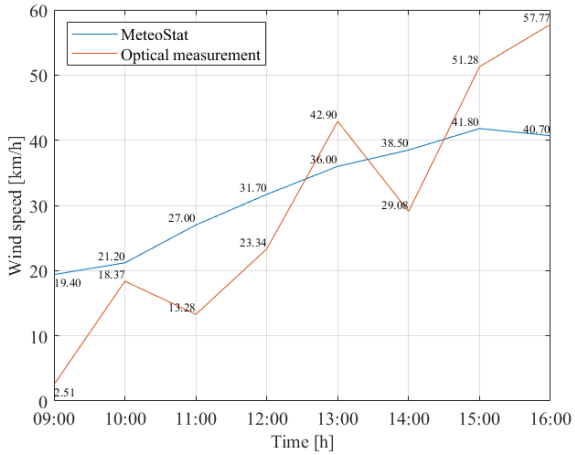

Figure 9. Evolution of the average apparent velocity and anemometric speed during the day of February 13, 2025.

The amplitude of the fluctuations is more pronounced in the downstream plume, which results in more intense turbulence and explains the higher measured velocity in this area.
From 12 noon onwards, the velocity field is mainly observed within the upstream plume. The increase in velocity promotes dissipation of the flow. In addition, the optical measurement shows that the velocity increases from 1 p.m. onwards, reaching speeds greater than or equal to 30 km/h.

Figure 8 also illustrates the air directions in the 2D plane of the image. Overall, the directions indicate a wind coming from the west, since the camera is facing south. This approximate direction is consistent with meteorological data indicating a predominantly westerly wind direction.
In the case of our application, the directions indicated by the optical method also reflect the interaction between the warm air in the plume and the cooler ambient air. The 9 a.m. measurement shows that the plume downstream first moves upward under the effect of heat, then downward as it cools. The 10 a.m. and 11 a.m. measurements also show that the air moves downward as its speed decreases. From 1 p.m. onwards, the directions are heterogeneous due to strong turbulence in the exhaust air.

3.2 Measurement of air velocity between buildings

The optical analysis of fog movement is based on a video sequence dated May 16, 2025.
The movement of fog under the effect of wind allows us to estimate its speed between buildings. The sequence studied shows a flow coming from behind the building in the foreground of the image and moving toward the camera.

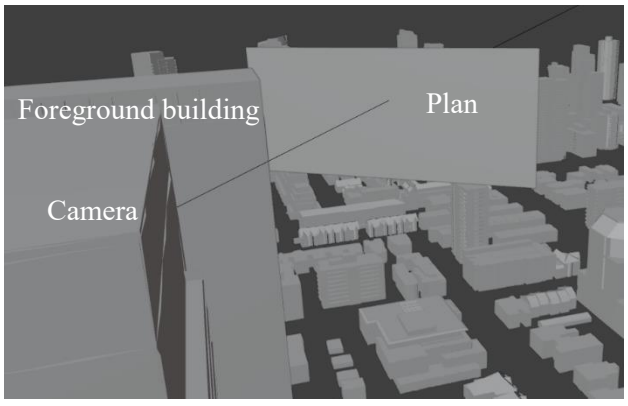

Figure 10. Modelling a virtual plane to measure fog displacement in the camera's field of view.

In the 3D model, a reference plane is introduced with a normal perpendicular to the wind direction recorded by the weather station, see Figure 10. Projecting the image onto this plane allows scale ratios to be established in [km/pixel].

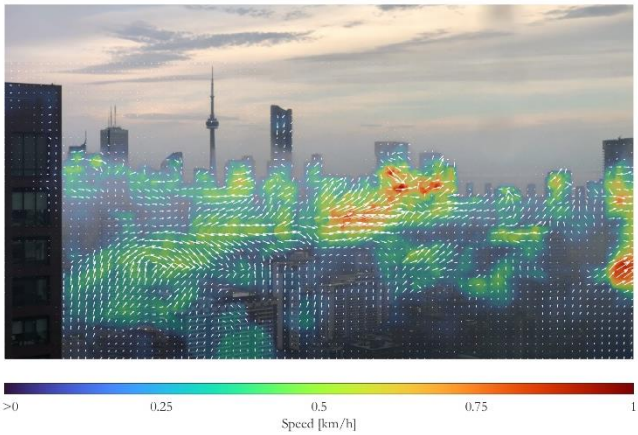

Figure 11. Air velocity and direction around buildings.

Figure 11 shows that the velocity field has an amplitude between 0.2 and 1 km/h. The velocity peaks are located above the flow and on the right side of the observation field.
Weather data for the recording period indicate a wind speed of 9 km/h. This difference reflects the complexity of the airflow field in urban environments. The optical measurement highlights the apparent movements of fog particles in the immediate vicinity of building facades, while the anemometric measurement records fluctuations in an area of lower density. Surrounding buildings cause local wind speed disturbances that can reduce flow speeds. Figure 11 also illustrates the dynamics of fog using the directions obtained by the optical method. Upward and downward movements result from the mixing of warm and cold air masses.

3.3 Discussion and perspectives

The experiments conducted in this paper rely on naturally occurring airborne particles to make local airflow patterns observable in the video sequence. Consequently, the analysis focuses on regions containing particles within the camera’s field of view.
In our study, the choice of exploiting a single point of view was a deliberate choice to focus on data density and information richness, from which a large number of flow vectors were extracted over time. In addition, the proposed approach is based on the fact that video data are not acquired through a dedicated measurement protocol. This highlights the ability to extract physically meaningful information from existing visual content, without requiring direct control over the acquisition process.
Next steps should assess the propagation of errors throughout the processing chain. In particular, the impact of uncertainties in the image projection onto the digital elevation model (DEM), numerical noise and image quality on the optical flow measurements should be quantified. Understanding these sources of uncertainty is crucial for evaluating the method’s robustness. Finally, further investigations should include a sensitivity analysis of window size and algorithmic parameter choices. Evaluating how these choices influence the final results will help to define best practices for applying the method to different urban configurations and imaging conditions.

This contribution has been peer-reviewed. The double-blind peer-review was conducted on the basis of the full paper.
https://doi.org/10.5194/isprs-annals-XI-3-2026-27-2026

4. Conclusions

This paper presents a proof-of-concept experiment to measure air velocity and direction from a video taken in an urban environment. The method proposes to bypass the need for *in situ* data collection by using freely available online content. We show that, in addition to providing realistic velocity estimates, the optical method can be used to study the dynamics of air movement. The use of a 3D model makes it possible to express the speed of flows in a physical speed unit comparable to the instrumental measurements of a weather station. It also makes it possible to discriminate between speed fields according to the depth of the scene. The method therefore covers a wide field of observation of flows in urban environments.
This work paves the way for other applications related to the assessment of air movements in urban environments, such as the measurement of the surface convective coefficient or the analysis of the airflow entering and leaving openings. These measurements could be carried out using a wider variety of content, such as images recorded by surveillance cameras or drones equipped with on-board cameras.

References

Allard, F. and Ghiaus, C. eds., 2012. *Natural ventilation in the urban environment: assessment and design*. Routledge.

Allwine, K.J., Shinn, J.H., Streit, G.E., Clawson, K.L. and Brown, M., 2002. Overview of URBAN 2000: A multiscale field study of dispersion through an urban environment. *Bulletin of the American Meteorological Society*, *83*(4), pp.521-536.

Anandan, P., 1989. A computational framework and an algorithm for the measurement of visual motion. *International Journal of Computer Vision*, *2*(3), pp.283-310.

Cao, Y., Mo, Z., Ai, Z., Wang, H. and Xiao, L., 2016. An efficient and visually accurate multi-field visualization framework for high-resolution climate data. *Journal of Visualization*, *19*(3), pp.447-460.

Carrega, P., 2008. Le vent: importance, mesures, modélisation et tribulations. *Bulletin de la Société géographique de Liège*, *51*, pp.17-29.

Carrillo, Alejandra. (2025,13 february). Toronto Timelapse 13 Feb 2025 [YouTube video]. YouTube. https://www.youtube.com/watch?v=PtacAvpx1v4

City of Toronto. (n.d.). *Creating a new state-of-the-art city model*. https://www.toronto.ca/business-economy/partnerships-sponsorships-donations/partner-2/partnership-stories/creating-a-new-state-of-the-art-city-model/

Fezzani, R., 2011. *Approche parallèle pour l'estimation du flot optique par méthode variationnelle* (Doctoral dissertation, Université Pierre et Marie Curie-Paris VI).

Gál, T. and Unger, J., 2009. Detection of ventilation paths using high-resolution roughness parameter mapping in a large urban area. *Building and Environment*, *44*(1), pp.198-206.

Georgakis, C. and Santamouris, M., 2006. Experimental investigation of air flow and temperature distribution in deep urban canyons for natural ventilation purposes. *Energy and buildings*, *38*(4), pp.367-376.

Hagishima, A. and Tanimoto, J., 2003. Field measurements for estimating the convective heat transfer coefficient at building surfaces. *Building and environment*, *38*(7), pp.873-881.

Hargather, M.J., Lawson, M.J., Settles, G.S. and Weinstein, L.M., 2011. Seedless velocimetry measurements by schlieren image velocimetry. *AIAA journal*, *49*(3), pp.611-620.

Holst, J. and Mayer, H., 2011. Impacts of street design parameters on human-biometeorological variables. *Meteorologische Zeitschrift*, *20*(5), p.541.

Horn, B.K. and Schunck, B.G., 1981. Determining optical flow. *Artificial intelligence*, *17*(1-3), pp.185-203.

Ingenhorst, C., Jacobs, G., Stößel, L., Schelenz, R. and Juretzki, B., 2021. Method for airborne measurement of the spatial wind speed distribution above complex terrain. *Wind Energy Science*, *6*(2), pp.427-440.

Kegerise, M.A. and Settles, G.S., 2000. Schlieren image-correlation velocimetry and its application to free-convection flows. In *Int. Symp. on Flow Visualization*.

Liu, C., 2009. *Beyond pixels: exploring new representations and applications for motion analysis* (Doctoral dissertation, Massachusetts Institute of Technology).

Liu, C., Freeman, W.T., Adelson, E.H. and Weiss, Y., 2008, June. Human-assisted motion annotation. In *2008 IEEE Conference on Computer Vision and Pattern Recognition* (pp. 1-8). IEEE.

Lucas, B.D. and Kanade, T., 1981, August. An iterative image registration technique with an application to stereo vision. In *IJCAI'81: 7th international joint conference on Artificial intelligence* (Vol. 2, pp. 674-679).

Oke, T.R., Mills, G., Christen, A. and Voogt, J.A., 2017. *Urban climates*. Cambridge university press.

Palyvos, J.A., 2008. A survey of wind convection coefficient correlations for building envelope energy systems' modeling. *Applied thermal engineering*, *28*(8-9), pp.801-808.

Patrikar, J., Moon, B.G. and Scherer, S., 2020, October. Wind and the city: Utilizing uav-based in-situ measurements for estimating urban wind fields. In *2020 IEEE/RSJ International Conference on Intelligent Robots and Systems (IROS)* (pp. 1254-1260). IEEE.

Pu, H., Chen, X., Yang, Y., Tang, R., Luo, J., Wang, Y. and Mu, J., 2023. Tassel-YOLO: A new high-precision and real-time method for maize tassel detection and counting based on UAV aerial images. *Drones*, *7*(8), p.492.

Rehman, S., 2014. Tower distortion and scatter factors of co-located wind speed sensors and turbulence intensity behavior. *Renewable and Sustainable Energy Reviews*, *34*, pp.20-29.

Settles, G.S., 1997. Visualizing full-scale ventilation airflows.